# Fabrication and Characterization of Polymer Hollow Microneedle Array Using UV Lithography Into Micromolds

Po-Chun Wang, Seung-Joon Paik, Shuodan Chen, Swaminathan Rajaraman, Seong-Hyok Kim, and Mark G. Allen, *Fellow, IEEE*

***Abstract*—Drug delivery through micromachined needles is an attractive alternative to intramuscular and subdermal injection by hypodermic needles, due to the potential for reduced pain caused by the micro-sized needles. In this paper, a polymer-based fabrication process using UV lithography into micromolds is developed, allowing the fabrication of microneedle (MN) shafts, tips, lumens, and substrate baseplate using lithography. Using UV lithography into micromolds allows complex three-dimensional structures to be defined, since both mask patterns and mold topography are available to define the structures. A hollow MN array and baseplate, in which the needle lumens extend through the thickness of the baseplate, are demonstrated. Fabricated SU-8 MNs are 825 $\mu$m in height and 400 $\mu$m in width, with a pyramidal tip; the needle lumen, 120 $\mu$m in diameter, intersects with one of the faces of the pyramidal tip. Mechanical characterization of the fabricated MNs shows that the fracture force of a single needle against a rigid surface is 12.0 N. The insertion force of a single needle into porcine skin is empirically determined to be 2.4 N. The fracture force of the needle against porcine skin is observed to be in excess of 90 N. [2012-0359]**

***Index Terms*—UV lithography, Micromolding technology, SU-8 photoresist, microneedle array.**

## I. Introduction

DRUG delivery through micromachined needles is of great interest to transport therapeutic agents, virus-like-particles, and other molecules into the body through the skin with minimal invasiveness and pain. Drug delivery with microneedles (MNs) has been shown to induce immune responses or biological effects that are comparable to those induced by a hypodermic needle (HN) injection in animal studies with influenza, Hepatitis B, Hepatitis C, and diabetes. [1]–[3] In addition, one human study with influenza reported that the influenza vaccines delivered with MNs produced immune responses similar to those from an HN vaccination.[4]

To deliver drugs into skin, MNs are typically first pressed perpendicularly against skin, resulting in the rupture of the outermost layer of skin, the stratum corneum (SC). The SC has a typical thickness of 10–20 $\mu$m in human skin and forms a substantial barrier to essentially all high-molecular-weight drugs. [5], [6] Underneath the SC are the viable epidermis (VE) of 50–100 $\mu$m thickness, and the dermis with a thickness of 1–2 mm. With the rupture of the SC, pathways to the VE or upper dermis (UD) are created by the penetration of MNs, followed by the delivery of drugs to the VE or UD. In addition to the reduced-pain insertion of MNs reported in human studies, potential advantages of MNs include blood-free insertion, minimal skin trauma, non-skilled/self-administration, reduced risk of needle-stick injury, and ease of disposal. [6], [7].

MNs can be categorized into two groups according to the existence of the lumen: Solid microneedles (SMNs) and hollow microneedles (HMNs). HMNs allow aqueous drugs to flow through the lumen and into the skin, leading to faster rates of drug delivery than SMNs that rely on the diffusion of drugs in the skin [1]. Fig. 1shows schematic illustrations of an HMN system as well as the drug delivery into skin through the HMN system. Moreover, with HMNs, it is possible to deliver drugs to a well-defined depth in the skin, and the depth can be controlled by the location of the lumen opening. Well controlled drug delivery over time, e.g., an intermittent delivery, is possible by steering the flow rate with a syringe or pump [8]. However, the fabrication of HMNs typically involves a more elaborate process than that of SMNs because of the need to construct the lumen.

Several microfabrication approaches have been reported to successfully construct the lumen of HMNs. Laser micromachining is commonly employed to create three-dimensional (3-D) structures. HMN structures have been obtained using the laser micromachining technique to fabricate the entire needle structure [9], to remove the lumen material from a pre-constructed SMN [10], [11], or to create a negative mold for the subsequent electroplating step where HMNs were defined [12]. HMNs with a height of 400–900 $\mu$m have been reported with laser micromachining.

Manuscript received November 28, 2012; revised January 30, 2013 and April 1, 2013; accepted April 5, 2013. Date of publication June 28, 2013; date of current version September 27, 2013. This work was supported in part by the National Institutes of Health under Grants R01-EB006369 and 1U01AI074579. Subject Editor Y. Zohar.

P. Wang, S.-J. Paik, S. Chen, and M. G. Allen are with the School of Electrical and Computer Engineering, Georgia Institute of Technology, Atlanta, GA 30332 USA (e-mail: pwang36@gatech.edu; spaik8@mail.gatech.edu; shuodan.chen@ece.gatech.edu; mark.allen@ece.gatech.edu).

S.-H. Kim was with the School of Electrical and Computer Engineering, Georgia Institute of Technology, Atlanta, GA, USA. He is now with L.G. Electronics, Seoul 150-721, Korea (e-mail: seonghyok.kim@gmail.com).

S. Rajaraman was with the School of Electrical and Computer Engineering, Georgia Institute of Technology, Atlanta, GA, USA. He is now with Axion BioSystems, Atlanta, GA 30332 USA (e-mail: srajaraman@axionbio.com).

Color versions of one or more of the figures in this paper are available online at http://ieeexplore.ieee.org.

Digital Object Identifier 10.1109/JMEMS.2013.2262587

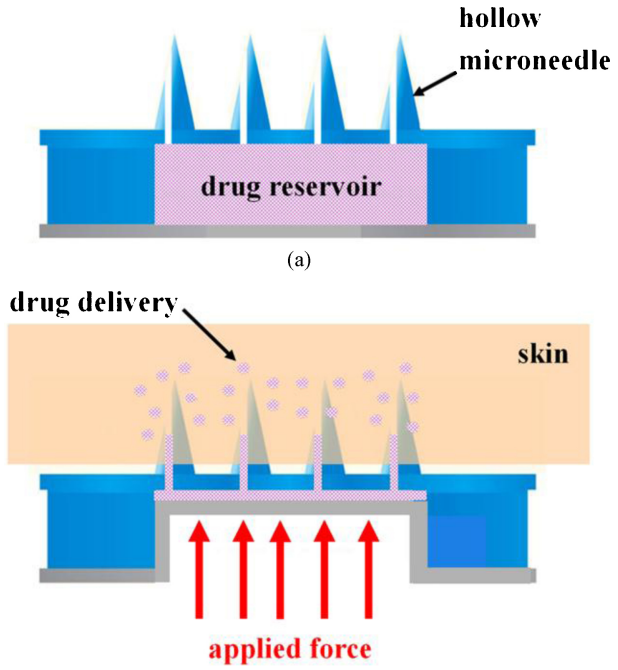


Fig. 1. (a) A schematic depiction of a hollow microneedle system, consisting of a hollow microneedle array and a drug reservoir. (b) An illustration of administration of drug delivery using the hollow microneedle system.

Silicon-based MEMS techniques are widely used to fabricate HMNs with a sub-micron tip. The lumen of these HMNs is often constructed using a deep-reactive-ion-etching (DRIE) technique. To form the shape of HMNs, several fabrication approaches, including anisotropic wet etching [13], isotropic dry etching [14], [15], a combination of isotropic and anisotropic dry etching [16], as well as saw dicing [17], have been reported. A tip of less than 0.1 $\mu$m in radius has been demonstrated with silicon-based MEMS techniques, and the height of the fabricated HMNs ranges from 200 to 700 $\mu$m.

Deep X-ray lithography (DXRL) is utilized to construct polymethyl methacrylate (PMMA) HMNs with two exposure steps [18]. Nevertheless, to extend the lumen inside HMNs through the baseplate of the HMN array, two additional micromolding steps are required. PMMA HMNs with a height of 400 $\mu$m are created using DXRL and the micromolding technique.

Conventional photolithography combined with a micromolding technique has been reported to simplify the fabrication process of HMNs. This integrative fabrication approach involves a photosensitive polymer cast on top of a surface-micromachined silicon mold. The tip profile of the HMNs is defined by the topography of the silicon mold, and the conventional photolithography is performed to construct the shaft and lumen of the HMNs as well as the baseplate. With this fabrication approach, HMNs with a height of 400–600 $\mu$m have been demonstrated [19]–[21]. Moreover, volcano-like HMNs have been constructed using drawing lithography [22] and solvent casting [23] with a height of 2 mm and 250 $\mu$m, respectively.

With these successes in the fabrication of HMNs, to make the manufacturing of HMNs appropriate for single-use devices several process features are required for HMN manufacturing.

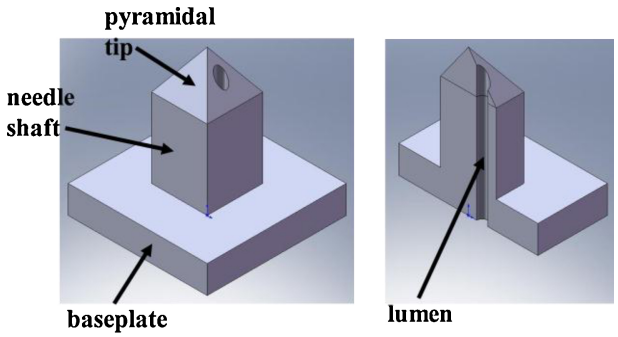


Fig. 2. (a) A depiction showing the desirable hollow microneedle structure with a baseplate. (b) A cross-sectional view of the hollow microneedle structure, showing that the lumen has two openings connecting the back of the baseplate to the top of the pyramidal slope.

Batch processing allows for high throughput and is scalable for high-volume production. Conventional photolithography is inherently batch processing in nature and therefore is desirable for HMN manufacturing. Moreover, the fabrication method of interest needs to be capable of creating 3-D structures for the construction of out-of-plane HMNs. In addition to creating 3-D structures, definition of a high-aspect-ratio lumen that forms a microfluidic channel between the tip of the HMN and the back of the baseplate is of great importance in the design of the fabrication approach for HMN manufacturing. Furthermore, the cost of manufacturing needs to be taken into consideration. The manufacturing cost can be reduced with the use of potentially low-cost materials, e.g., polymers, for the structure material of the HMNs and the baseplate as well as by refraining from costly processing and facilities.

To meet the required process features for HMN manufacturing, a polymer-based fabrication process using ultraviolet (UV) lithography into micromolds has been developed and an HMN array with a baseplate was demonstrated [24]. Using UV lithography into micromolds allows complex 3-D structures to be defined with both the mask pattern in the lithography process and the topography of the micromold. In this paper, with a pre-constructed reusable mold defining the tip of HMNs, the shaft and lumen of the needles as well as a baseplate are all fabricated using a UV-sensitive polymer, i.e., SU-8, in a dual-exposure lithography process. This conventional UV lithography technique, widely used in the microelectronics industry [25], is batch-compatible and potentially scalable to high volumes. This integrative fabrication process utilizes potentially low-cost polymer materials, i.e., SU-8 for the HMN structure and polydimethylsiloxane (PDMS) as the micromolding material. Furthermore, UV lithography and micromolding methods are expected to have low mass production costs [5]. The flexibility of PDMS as a molding material is expected to facilitate the demolding processing.

Fig. 2 shows schematic depictions of the desirable HMN structures in this paper. This HMN has three major components: A top pyramidal tip, a square shaft, and a baseplate. The lumen of the HMN has two openings: One is on the pyramidal slope, and the other is located on the bottom side of the baseplate. The fabrication and mechanical characterization

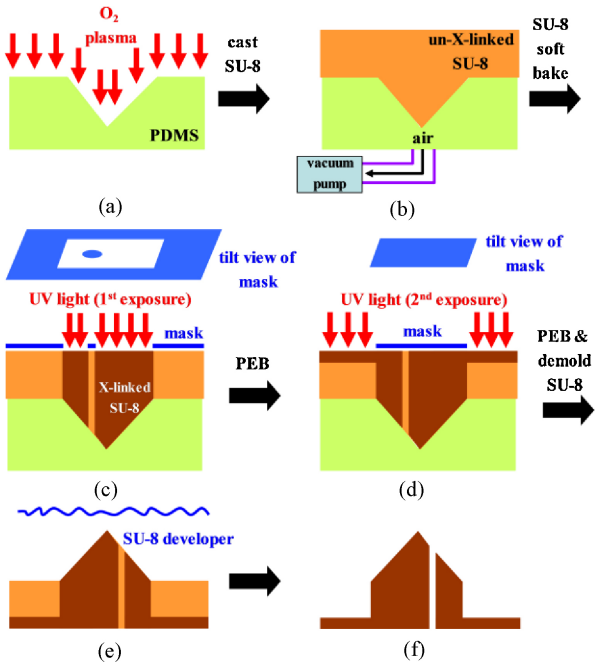


Fig. 3. Fabrication process flow for the hollow SU-8 microneedle array.

of the HMN of interest as well as its insertion performance into excised animal skin are discussed in this paper.

## II. Fabrication Process Development

A schematic process flow for the fabrication of SU-8 HMNs using UV lithography into PDMS micromolds is shown in Fig. 3. In this process flow, SU-8 is cast onto a pre-constructed PDMS mold (Fig. 3a and Fig. 3b), followed by the softbake of SU-8. The subsequent two UV-exposure steps with different dosages and separate masks define the HMN structure and a baseplate, as shown in Fig. 3c and Fig. 3d, respectively. The entire structure of the SU-8 master is demolded from the PDMS mold, followed by the development of SU-8 (Fig. 3e) to create the SU-8 HMN with a baseplate (Fig. 3f). The fabrication process and its processing parameters/conditions are described in detail in Subsection III.A.

To make the process of using UV lithography into micromolds manufacturable, several fabrication issues associated with UV lithography and the micromolding technique in general need to be addressed, including air bubbles trapped between the photosensitive material and the mold, internal reflection of UV light at the interface between these two materials, and thermal expansion of the polymer mold in the baking process of the photosensitive material. Moreover, an additional baking step is added to facilitate the subsequent alignment through the thick photosensitive material.

### A. Elimination of Trapped Bubbles by Back-Side Vacuuming

With SU-8 preheated at 60 °C and the PDMS mold treated using oxygen plasma for better encapsulation of the microtrenches, a significant number of air bubbles were still observed at the bottom of the PDMS trenches following the casting of SU-8 onto the PDMS mold, as shown in Fig. 4a.

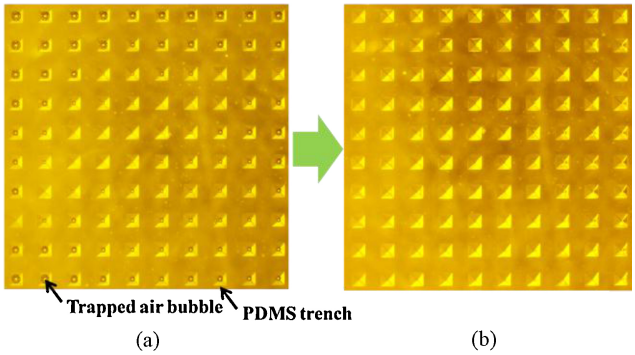


Fig. 4. Optical micrographs of the top view of the SU-8/PDMS sample in Fig. 3b before (a) and after (b) the backside vacuuming process. (a) More than 50 air bubbles of various dimensions trapped at the bottom of the PDMS trenches. (b) Elimination of the trapped air bubbles.

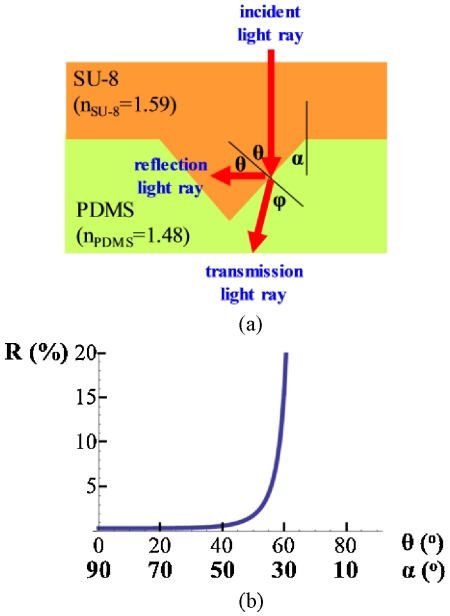


Fig. 5. (a) A schematic illustration of different UV rays at the SU-8/PDMS interface and their corresponding angles to the normal of the interface. (b) A chart of the reflection coefficient (R) as a function of the incident angle ($\theta$) and the inclined angle of the PDMS trench ($\alpha$).

To eliminate these air bubbles, the SU-8/PDMS sample was placed at the center of a rubber plate where there is an opening connected to a vacuum pump. Because of the gas permeability of PDMS [26], the air trapped at the bottom of the PDMS trenches was pulled through the PDMS mold and subsequently removed by the vacuum pump, as shown in Fig. 3b. An optical micrograph of the top side of the SU-8/PDMS sample following a 3-h backside vacuuming (BSV) process is shown in Fig. 4b, and no air bubble is observed at the bottom of the PDMS trenches under an optical microscope.

### B. Internal Reflection at the Interface

In addition to the intended exposure shown in Fig. 3c, undesirable exposure may occur because of the reflection of UV light at the SU-8/PDMS interface shown in Fig. 5a. This reflected light is a result of the mismatch in the refractive indices of SU-8 and PDMS. This exposure of SU-8 may

lead to undesired crosslinking in the lumen, inhibiting flow through the lumen.

To estimate the intensity of the reflected UV light from the SU-8/PDMS interface with different incident angles, the law of reflection, Snell's law of refraction, and Fresnel's equations were used [27]. Fig. 5a shows a schematic illustration of different UV rays at the SU-8/PDMS interface and their corresponding angles to the normal of the interface. Given that the refractive indices of SU-8 and PDMS are 1.59 and 1.41 [28], [29], respectively, the transmission angle ($\varphi$) can be expressed as a function of the incident angle ($\theta$) using Snell's law. The reflection coefficient ($R$), defined as the ratio of the intensity of the reflected UV light to that of the incident UV light, can be determined using Fresnel's equations:

$$R = \frac{R_{\mathrm{TM}} + R_{\mathrm{TE}}}{2} \tag{1}$$

where

$$R_{\mathrm{TM}} = \frac{\tan^2(\theta - \varphi)}{\tan^2(\theta + \varphi)}$$

and

$$R_{\mathrm{TE}} = \frac{\sin^2(\theta - \varphi)}{\sin^2(\theta + \varphi)}.$$

Fig. 5b shows the calculated reflection coefficient ($R$) plotted as a function of the incident angle ($\theta$) and the inclined angle of the PDMS trench ($\alpha$). As shown in Fig. 5b, a smaller incident angle ($\theta$) leads to less UV reflection from the interface. Therefore, the inclined angle of the trenches in the PDMS mold was carefully considered. To reduce the reflection coefficient below 5%, the inclined angle of the PDMS trench was chosen to be 35°.

### *C. Compensation for the Thermal Expansion of a Polymer Mold With Photomask Design*

In the SU-8 softbake process, the elevated temperature on the hotplate caused the solid PDMS mold to expand while the SU-8 in liquid state was being stretched horizontally along the PDMS mold. Fig. 6a shows a schematic depiction of the top view of the SU-8/PDMS sample with a $10 \times 10$ array of PDMS trenches. Schematic depictions of the cross-sectional view of one side of the SU-8/PDMS sample prior to and after the softbake process are shown in Fig. 6b and Fig. 6c, respectively.

Since the location of the needle shaft is defined by the mask pattern on the photomask and that of the needle tip is determined by the PDMS trench in the first UV exposure step as shown in Fig. 3c, to construct a well-defined MN structure the alignment between the mask pattern and the PDMS trench is of importance. Therefore, with the dimension of the PDMS mold increased in the softbake process, the first UV exposure with a set of mask patterns designed based on the mold dimension prior to the softbake process resulted in a shift between the needle shaft and tip as shown in Fig. 6d. The shift is maximum for outmost needles in the needle array.

To eliminate this undesirable shift in the MN structure, the thermal expansion of the PDMS mold in the softbake process was taken into consideration during the design process of the photomask. With a newly-designed mask pattern

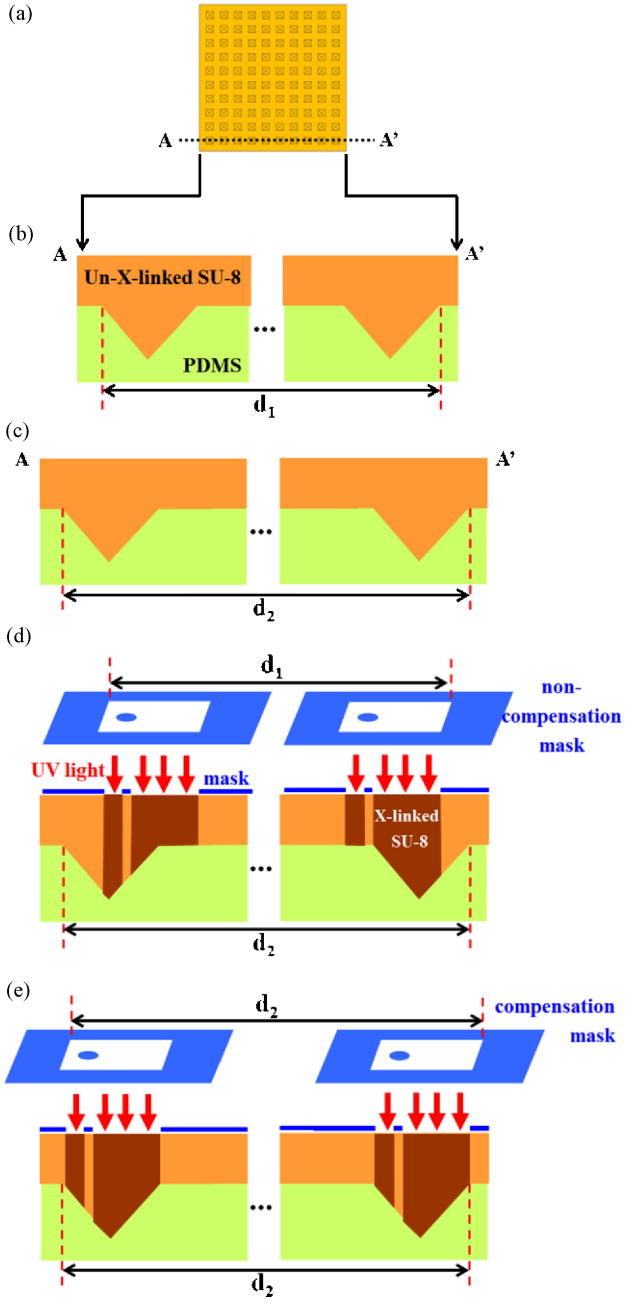


Fig. 6. Schematic illustration of the thermal expansion of the PDMS mold. (a) A schematic depiction of the top view of the SU-8/PDMS sample. The PDMS trenches in a $10 \times 10$ array are visible through the SU-8. (b) A schematic depiction of the cross-sectional view of one side (A-A' in (a)) of the SU-8/PDMS sample prior to the softbake process. The ten PDMS trenches on one side of the SU-8/PDMS sample are represented by the leftmost and rightmost ones. (c) A depiction of the sample after the softbake process, showing the thermal expansion of the PDMS mold. (d) An illustration of the SU-8/PDMS sample exposed with a non-compensation photomask in the first UV exposure process. (e) An illustration of the sample exposed with a compensation mask in the first UV exposure process.

whose dimension was designed to compensate for the thermal expansion of the PDMS mold, the location of the mask pattern is aligned with the PDMS trenches, resulting in a well-defined needle structure, as shown in Fig. 6e. As shown in Fig. 6d and Fig. 6e, the desired formation of the needle structure relies on the good lateral alignment between the photo mask and the PDMS trenches. The patterns are insensitive to thermal

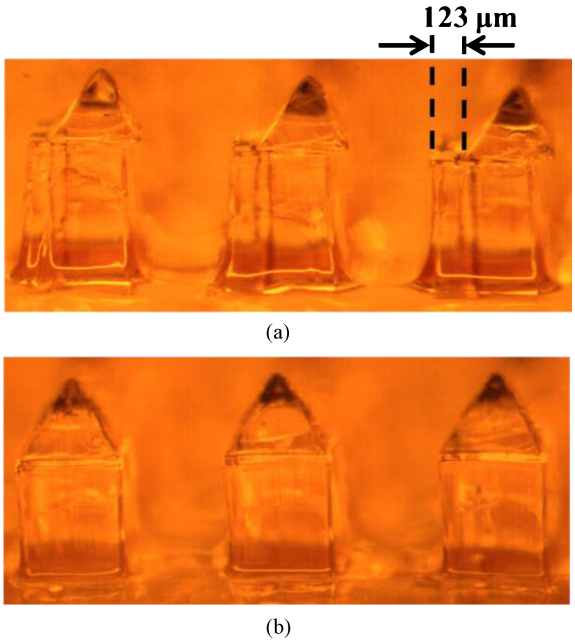


Fig. 7. (a) An optical micrograph of the rightmost three microneedles of the sample shown in Fig. 6d. The shift between the needle tip and shaft is 123 $\mu$m for the rightmost needle. (b) An optical micrograph of the rightmost three needles of the sample shown in Fig. 6e. No significant shift between the needle tips and the shafts is observed.

mismatch in the vertical direction, since the incident UV light shines along the vertical direction.

To design the new photomask to compensate the thermal expansion of the PDMS mold in the softbake process, this expansion was estimated with the equation of linear thermal expansion [30]

$$\frac{\Delta L}{L_0} = \alpha_L \Delta T \tag{2}$$

where $L_0$ is the initial length, $\Delta T$ the temperature change of the object, $\Delta L$ the change in the length of the object, and $\alpha_L$ is the coefficient of linear thermal expansion. With the $\alpha_L$ of $3.1 \times 10^{-4}$ $(°C)^{-1}$ for PDMS [31], $\Delta T$ of 95 °C for the temperature increase from 25 to 115 °C, and $L_0$ of 3800 $\mu$m for the distance from the center to the rightmost or leftmost point of the 10 PDMS trenches, which is half of $d_1$ shown in Fig. 6b, the thermal expansion for the right or left five trenches was estimated to be 106 $\mu$m. The photomask pattern was thus adjusted throughout the entire array to compensate the thermal expansion of the PDMS mold.

Fabricated MNs with different photomasks used in the first UV exposure step are shown in Fig. 7 for comparison. Fig. 7a shows an optical micrograph of the rightmost three MNs of the sample in Fig. 6d fabricated with a non-compensation photomask. A shift of 123 $\mu$m between the needle tip and shaft was observed in the rightmost needle. Meanwhile, Fig. 7b shows the rightmost three needles of the sample in Fig. 6e fabricated with a compensation photomask and no significant shift was observed. Similar results were observed with the leftmost three needles of the samples shown in Fig. 7. Therefore, with the newly-designed photomask the thermal expansion of the PDMS mold in the softbake process can be compensated to construct well-defined MN structures.

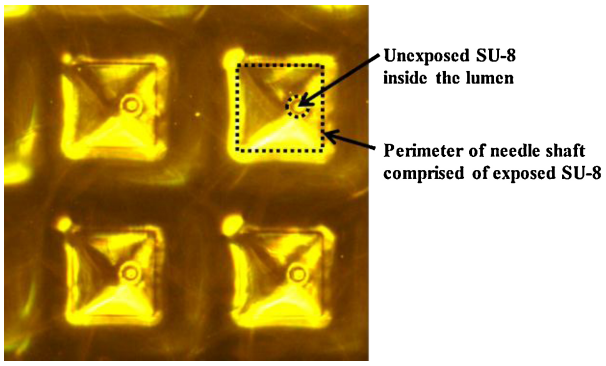


Fig. 8. An optical micrograph of the top view of the SU-8/PDMS sample in Fig. 3c following the first post-exposure-bake step. Four needles in an array of two-by-two are shown. A clear image of the perimeter of the exposed SU-8 because of the first PEB step on the top surface of the SU-8 is visible and serves as an alignment mark in the subsequent alignment for the second exposure process.

The utilized compensation scheme was solely based on the thermal expansion of the PDMS substrate, as opposed to considering the detailed thermal expansion characteristics of the PDMS/SU-8 composite. This approach yielded significant improvement in needle alignment over the entire needle array over no compensation as demonstrated in Fig. 7. However, some alignment error was still observed, which could be addressed by refined compensation schemes. Further compensation could be achieved, e.g., by considering the cooling of the SU-8/PDMS composite after softbake between the glass transition temperature ($T_g$) of uncrosslinked SU-8 (50 °C [32]) and room temperature (the temperature at which lithographic exposure took place). Such refined compensation schemes may become more important when considering large area manufacturing of multiple arrays.

### *D. Two PEB Steps for a Dual-Exposure Process*

The alignment between the photomask and the perimeter of the PDMS trench during the two exposure processes (Fig. 3c and Fig. 3d) presents a technical difficulty, since the alignment is performed between two objects with a vertical distance of 800 $\mu$m, which is the thickness of the SU-8.

To prevent this alignment difficulty during the second exposure process (Fig. 3d), a PEB step was performed following the first UV exposure step. With the addition of this PEB step the boundary between exposed and unexposed SU-8 became visible under the aligner optical microscope. Fig. 8 shows an optical micrograph of the top view of the SU-8/PDMS sample following this PEB step. The perimeter of the exposed SU-8 needle shaft, which is a boundary between exposed and unexposed SU-8, is visible as shown in Fig. 8 and serves as an alignment mark during the subsequent alignment for the second UV exposure. The alignment difficulty was significantly reduced for the second exposure process, since the alignment of the photomask was performed to the alignment mark on the top surface of the SU-8, instead of to the perimeter of the PDMS trench at the bottom of the SU-8 layer.

Moreover, since the second UV lithography process (Fig. 3d) is to define the baseplate that locates on the top of the SU-8, the function of the PEB step following the second

UV exposure is to provide thermal energy to the top of the SU-8. Compared to a hotplate where the thermal energy is supplied to the bottom of the SU-8/PDMS sample, in an oven the thermal energy is provided to the top surface of the SU-8 where the top surface is in direct contact with the heated air. Therefore, the second PEB step was performed in an oven to define the baseplate on the top of the SU-8.

## III. Microneedle Fabrication

With several fabrication issues associated with UV lithography and the micromolding technique successfully addressed, the fabrication approach using UV lithography into micromolds was utilized to create HMNs with a baseplate.

### A. Fabrication Process of HMNs

The fabrication process of the HMN array consists of two steps. The first step is the construction of an intermediate PDMS mold with pyramidal trenches on the top surface, which define the profile of the MN tip. To construct the intermediate PDMS mold, an inclined UV lithography technique [33], [34] was used to create pyramidal trenches on the top surface of an SU-8 sample. Following the Cr/Au coating of the SU-8 sample, PDMS (Sylgard 184, Dow Corning, Midland, MI, USA) was cast onto the SU-8 sample and cured at room temperature for two days to obtain a positive PDMS master. The positive PDMS master was subsequently coated with Cr/Au, followed by casting of another PDMS onto this master to create a negative PDMS mold. The intermediate PDMS mold was obtained by demolding the negative PDMS mold from the positive PDMS master. Detailed description of the construction of the intermediate PDMS mold was reported in [35], [36].

The second step is the fabrication of the hollow SU-8 MN on the constructed intermediate PDMS mold and is shown in Fig. 3. SU-8 2025 (MicroChem Corp., Newton, MA, USA) was first preheated at 60 °C on a hotplate for 30 min to improve its encapsulation of the micro-trenches by reducing its viscosity. Oxygen plasma with a RF power of 300 W was used to treat the top surface of the intermediate PDMS mold for 20 min, yielding a more hydrophilic surface for better encapsulation of the micro-trenches (Fig. 3a). The SU-8 was cast by weight to obtain a thickness of 800 $\mu$m on the PDMS mold. To remove the bubbles trapped in the PDMS trenches with the integrity of the top surface of the SU-8 intact, a BSV process as shown in Fig. 3b was performed for 3 h. The SU-8/PDMS sample was subsequently softbaked on a level hotplate at 115 °C for 24 h. UV (365 nm I-line) lithography was utilized to define the HMN structure. Two direct UV exposure steps with separate photomasks to define the HMN and the baseplate are shown in Fig. 3c and Fig. 3d, respectively. In the first exposure (Fig. 3c), the pyramidal tip and shaft of the HMN were defined using a chromium mask, consisting of a $400 \times 400\ \mu m^2$ clear square region for the shaft and a dark circular pattern of 120 $\mu$m in diameter for the lumen. The UV dosage was 3000 mJ/cm$^2$. The first PEB step was subsequently performed with a hotplate at 115 °C for 30 min. The second exposure with a separate mask and a reduced dosage of 350 mJ/cm$^2$ defined the baseplate for the HMN array (Fig. 3d), followed by the second PEB step in an oven at 115 °C for 15 min to accommodate a certain thickness (100–200 $\mu$m) of the baseplate.

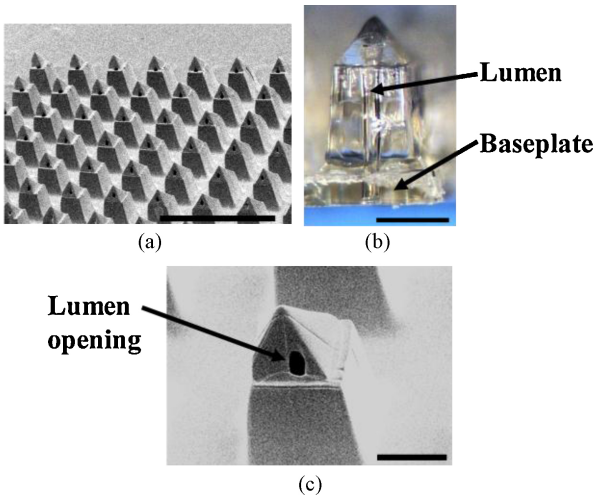


Fig. 9. (a) An SEM image of bird's-eye view of fabricated microneedle array coated by 15 nm Cr/150 nm Au for SEM imaging. (b) An optical micrograph showing a fabricated hollow microneedle with a baseplate. (c) An SEM image revealing the pyramidal tip with a lumen opening and upper shaft. The scale bar is 2 mm, 400 $\mu$m, and 250 $\mu$m in (a), (b), and (c), respectively.

Following the demolding of the SU-8 master from the intermediate PDMS mold, the development of the SU-8 master was performed in the propylene glycol methyl ether acetate (PGMEA) developer for 6 h in a static bath and additional 2 h in an ultrasonic bath (Fig. 3e). This additional 2-h development was to remove the clogging in the needle lumens. Following development, the SU-8 sample was rinsed with isopropyl alcohol (IPA) solution and blown dry with a nitrogen gun. After drying, the sample was inspected under an optical microscope. No physical damage to the cross-linked SU-8 was observed after development. Swelling of the SU-8 occurred to a small degree immediately after the development [37], and was reversed after overnight storage in the cleanroom. A completed SU-8 HMN with a baseplate is shown in Fig. 3f.

To enhance the mechanical strength of the SU-8 HMNs, a flood UV exposure step and a hardbake process were performed. The UV dosage in the flood exposure is 10 J/cm$^2$, and the hardbake process was carried out on a hotplate at 135 °C for 30 min.

### B. Fabrication Result

A fabricated HMN array is shown in Fig. 9. A scanning-electron-microscope (SEM) image of the bird's-eye view of the fabricated needle array is shown in Fig. 9a. The fabricated HMNs are in a $10 \times 10$ array at the center of a baseplate chip with a dimension of 25.6 mm $\times$ 25.6 mm. Fig. 9b shows an optical micrograph of an HMN with a baseplate. The height of the HMN is 825 $\mu$m, including a 255-$\mu$m tall pyramidal tip and a 570-$\mu$m tall shaft. The base width of the needle is 400 $\mu$m. An SEM image of the needle tip with a lumen opening is shown in Fig. 9c. The tip diameter measured using SEM ranges from 15 to 25 $\mu$m across the array [24].

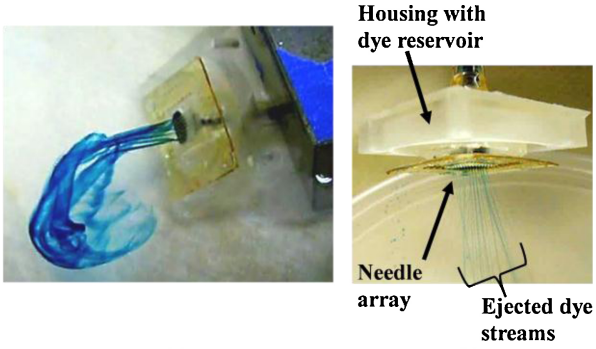


Fig. 10. (a) An optical picture showing the result of microfluidic characterization performed in fresh water. Streams of blue dye are being ejected from a microneedle array. (b) An optical picture illustrating that the blue dye is being emitted from the needle array, while the array is suspended in air with microneedles facing down.

### C. Microfluidic Channel Test

To characterize the microfluidic lumens of the fabricated HMN array, a custom fluidic test setup was used [24]. To examine the development and formation of the HMN lumens, the dye in the syringe was driven by a syringe pump to the backside of the baseplate of a $10 \times 10$ needle array and subsequently through any open HMN lumens. The microfluidic characterization was performed both in fresh water and in air. The ejection of the blue dye from the HMN array was observed while the array was either submersed in water or suspended in air as shown in Fig. 10a and Fig. 10b, respectively.

Visual examination of the fluidic ejection from the array suspended in air indicated that ~20 well-defined lumens were formed as shown in Fig. 10b. The other 80 lumens were occluded by an un-intended SU-8 film near the baseplate opening of the lumen. Diffraction underneath the photomask may cause undesired SU-8 exposure under the photomask [38] and result in the observed SU-8 film. The fluid pressure required to eject water through the needle array was measured with a manometer (Model 220, Netech, Farmingdale, NY, USA) to be less than 689.5 N/m$^2$ (0.1 pound per square inch), which is the minimum resolution of the manometer. Since the dimension of the baseplate chip is 0.0256 m $\times$ 0.0256 m (1.01 in. $\times$ 1.01 in.), the force required to eject water through the needle array is less than 0.45 N (0.1 pound-force). For comparison, the maximum force produced by a human thumb is 105 N (23.6 pound-force) [39].

Inspection of the needle tips and the baseplate under an optical microscope during the microfluidic characterization confirmed no crack formation in the baseplate. This alleviates concern that baseplate cracking is the reason for the observed microfluidic flow.

## IV. Characterization of Microneedles

### A. Preparation of Individual Microneedles

Characterization of HMNs was performed on individual single needles for simplicity. All HMNs were flood exposed with UV light and hardbaked as described in Subsection III.A. After the hardbake process, 15 nm of chromium and 150 nm of gold were sputtered onto the surface of MNs and the baseplate to create a conductive path between the tip of the MN and the perimeter of the baseplate. An individual needle with surrounding baseplate was then cut out of the needle array with a razor blade and placed on the bottom surface of a flat-head steel machine screw. Silver paint (Pelco® Conductive Silver 187, Ted Pella Inc., Redding, CA, USA) was dispensed to create a conductive path from a portion of the baseplate perimeter to the machine screw, completing the conductive path between the tip of the needle and the steel machine screw. This conductive path is required for the measurement of the insertion force, which is discussed in Subsection IV.C. The flat head of the machine screw was then affixed to the center of the plate of an aluminum SEM specimen mount for ease of handling. A copper wire was used to electrically connect the machine screw to the ohmmeter of a force–displacement apparatus for the measurement of the insertion force.

### B. Mechanical Characterization of Microneedle

MNs are commonly inserted into skin in a way that the needle shaft is perpendicular to the surface of the skin. Therefore, the skin exerts axial compressive force on the MN. To understand the mechanical response of an MN under axial compressive stress, a uniaxial compressive test was performed with individual MNs.

A force–displacement test station (Model 921A, Tricor Systems Inc., Elgin, IL, USA) was used to perform the uniaxial compressive test. In the test, the load cell of the test station drives an aluminum plate toward the MN and the surface of the plate is perpendicular to the shaft of the needle. The MN is held stationary. The load cell measures the force at the aluminum plate/needle interface and records the displacement of the plate. A 100 $\times$ microscope camera was used to record the video of the test. The aluminum plate was driven at a rate of 0.025 mm/s for video recording.

A representative force–displacement chart of the uniaxial compressive test for a single MN is shown in Fig. 11. The displacement of zero represents the initial contact between the aluminum plate and the MN tip. In Fig. 11, the force initially increases with the displacement and reaches the first peak at a displacement of 220 $\mu$m and decreases until reaching 250 $\mu$m displacement.

Four optical micrographs shown in Fig. 12a–d were taken at a displacement of 130, 200, 250, and 290 $\mu$m, respectively, to assess the integrity of the needle. Fig. 12a and Fig. 12d were taken with an optical microscope after the test was stopped at a displacement of 130 and 290 $\mu$m, respectively. Fig. 12b and Fig. 12c were captured from the video clip taken with the 100 $\times$ microscope camera during the test at a displacement of 200 and 250 $\mu$m, respectively.

Since Fig. 12a was taken when the external force from the aluminum plate was removed, the deformed tip of the MN suggests that the tip underwent plastic deformation as the force initially increased with the displacement. No crack at the needle tip was observed under an optical microscope at a displacement of 130 and 200 $\mu$m, as shown in Fig. 12a and Fig. 12b, respectively.

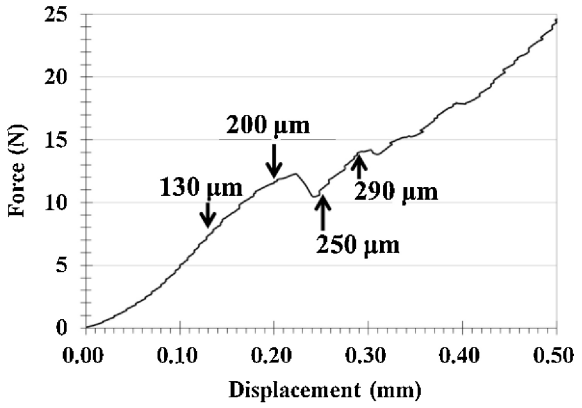


Fig. 11. A representative force-displacement chart in the uniaxial compressive test of a microneedle. The zero displacement represents the initial contact between the needle tip and the aluminum plate. The reaction force initially increases with the displacement and reaches the first peak value at a displacement of 220 $\mu$m and decreases until reaching 250 $\mu$m displacement.

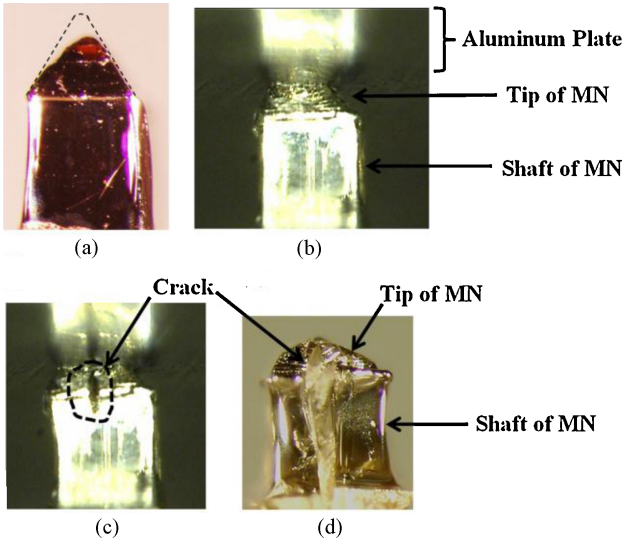


Fig. 12. Optical micrographs showing the side view of a microneedle at the four indicated points of Fig. 11 during the uniaxial compressive test. (a) An image of a needle taken after the test is stopped at a displacement of 130 $\mu$m. The dotted line represents the tip profile prior to the test. (b) An image of the aluminum plate and a needle captured from a video clip of the test. The displacement is 200 $\mu$m. (c) Another image captured from the same video clip. The displacement is 250 $\mu$m. A crack is observed at the needle tip. (d) An image of a needle taken after the test is stopped at a displacement of 290 $\mu$m. A large crack is observed and results in the splitting of the needle tip and shaft structures.

After the force reached the first peak at a displacement of 220 $\mu$m, a crack at the needle tip was observed in Fig. 12c at a displacement of 250 $\mu$m, and Fig. 12d shows a larger crack along the needle tip and shaft structures, causing the splitting of the needle. Therefore, the observation in Fig. 12 suggests that the cracking/fracture of the needle tip occurred between displacements of 200 and 250 $\mu$m. Since a decrease in force implies a failure in the structural integrity of the needle, the force at the first force peak is defined as the fracture force of the needle, at which the fracture of the needle tip occurs. The fracture force is 12.2 N in Fig. 11.

Fig. 13 shows a chart of the fracture force measured from five individual MNs in the uniaxial compressive test. The

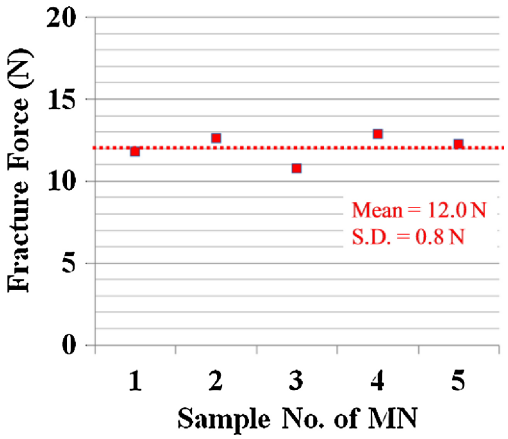


Fig. 13. A chart showing the fracture force of five individual microneedles measured in the uniaxial compressive test. The mean value of the fracture force is 12.0 N with a standard deviation of 0.8 N.

mean of the fracture force of these five MNs is 12.0 N with a standard deviation of 0.8 N.

Microscope observation of the five MNs in the uniaxial compressive test indicates that during the test a crack initially occurs at the needle tip and develops along the tip and shaft structures of the needle, leading to a vertical splitting of the needle. The failure mode of this vertical splitting of a structure under a uniaxial compressive test is called "axial splitting" [40]. This failure mode is common for unconfined brittle materials. The stress-strain curve of SU-8 after a hardbake indicates that hardbaked SU-8 is a brittle material [32], [41].

### C. Biological Insertion Characterization of Microneedle

To characterize the insertion performance of the fabricated HMNs into skin as well as to understand the subsequent mechanical interaction between the MN and skin, three investigations were conducted using excised porcine skin. The required driving force for a single MN to successfully insert into skin was first measured. Following the insertion into skin, the driving force that results in blunting the needle tip was estimated. Furthermore, the maximum driving force onto a MN without causing tip fracture was assessed.

1) *Preparation of Excised Porcine Skin:* The skin penetrability of the fabricated MNs was evaluated with excised porcine skin. The excised porcine skin (Pel-Freez, Rogers, AR, USA) was shaved using a razor and the subcutaneous fat on the back of the skin was subsequently removed with a scalpel. The prepared skin was affixed under mild tension to a wooden block using screws. Individual MNs were used to characterize the insertion performance of the needle into skin.

2) *Insertion Force Measurement of Single Microneedle:* To measure the insertion force, the needle was pressed perpendicularly against the porcine skin at a rate of 1.0 mm/s by the force–displacement test station described in Subsection IV.B, followed by separation of the needle from the skin.

During the process of pressing the needle against the porcine skin, the occurrence of the rupture of the SC, by which successful insertion is defined, can be detected with the measurement of the skin resistance [42]. Fig. 14 shows

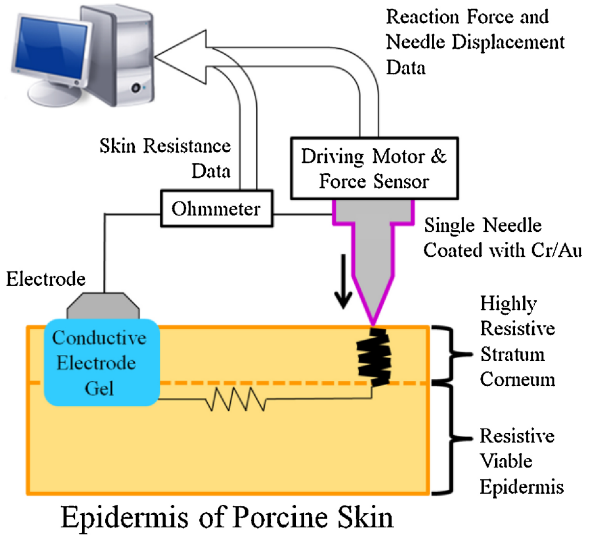


Fig. 14. A schematic diagram of the measurement setup of the insertion force for a microneedle. The SU-8 needle and baseplate are coated with a chromium/gold layer to complete the electrical circuit for the resistance measurement of the skin, which includes the highly-resistive stratum corneum and the resistive viable epidermis. During the insertion test, the data of the skin resistance is recorded in the computer of the test station simultaneously with the data of reaction force and needle displacement.

a schematic diagram of the measurement setup of the skin resistance as well as the measurement of the reaction force and needle displacement. The skin resistance, as shown in Fig. 14, consists of the resistances from the highly-resistive SC and the resistive VE, and therefore an abrupt decrease in the skin resistance can serve as an electrical indication of the rupture of the SC. The load cell of the test station presses the needle perpendicularly against the porcine skin and measures the reaction force from the needle. The force and displacement data are recorded by the computer of the test station, and simultaneously the ohmmeter measures the skin resistance and sends the data to the computer for recording. A representative chart of the skin resistance and the reaction force plotted as a function of the needle displacement is shown in Fig. 15. The abrupt decrease of the skin resistance at a displacement of 535 $\mu$m indicates the rupture of the SC. Therefore, the corresponding force of 1.5 N at a displacement of 535 $\mu$m is taken as the insertion force.

In the measurement of the insertion force, seven individual MNs were tested, and each needle was inserted into porcine skin an average of two times, yielding 15 data points for the estimation of the insertion force. Fig. 16 shows the measured insertion force plotted against the sample number of each MN. The mean of the measured insertion force is 2.4 N with a standard deviation of 1.2 N.

Following the separation of the needle from the skin, one drop of blue dye was dispensed onto the skin surface. The dye flowed through the MN-defined pathway in the SC and stained the VE underneath. Stain in the VE serves as a physical indication of successful insertion of the MN into skin. The skin surface was then wiped with alcohol swabs to remove the residual dye on the skin, followed by inspection of the skin under an optical microscope. An optical micrograph of

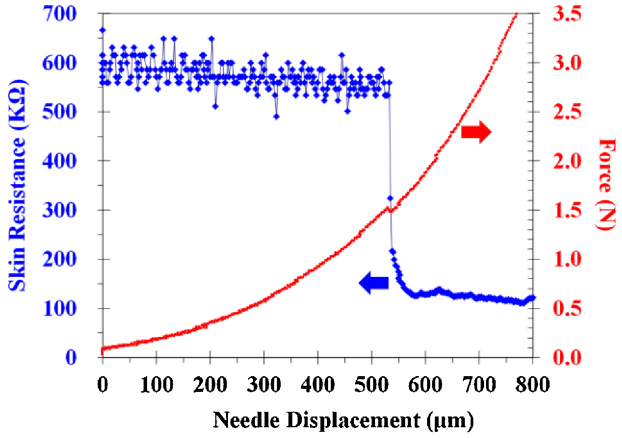


Fig. 15. A representative chart of the skin resistance and the reaction force plotted as a function of the needle displacement. The insertion force is defined as the corresponding force of 1.5 N at a displacement of 535 $\mu$m where the abrupt decrease of the skin resistance serves as an electrical indication of the rupture of the stratum corneum.

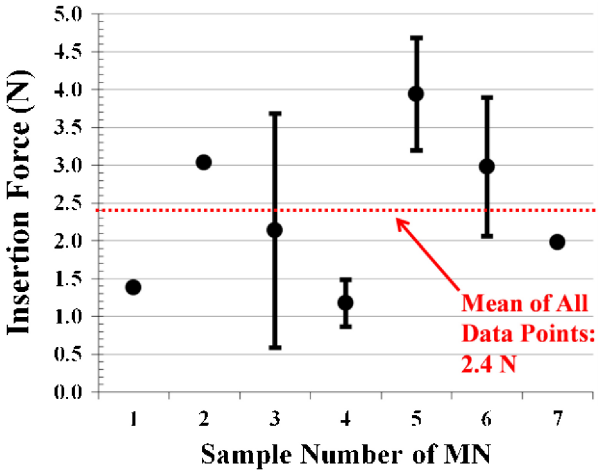


Fig. 16. A chart of the measured insertion force plotted against the sample number of microneedles. Seven individual MNs are tested. Microneedles with the sample number 1, 2, and 7 are tested one time, and needles with the number 3, 4, 5, and 6 are tested multiple times up to four times. The circle for each MN represents the mean of the measured insertion force with the MN, and the upper and lower whiskers are the standard deviations. There are 15 insertion tests in total performed with these 7 needles, and the mean of these measured insertion force is 2.4 N with a standard deviation of 1.2 N.

the top view of an insertion site is shown in Fig. 17. The inner red dotted line marks the opening in the SC created by the successful insertion of the MN into the porcine skin. The outer black dashed line outlines the underneath VE region that is stained by the dye.

3) *Tip-Blunting Force Estimation:* Observations in Fig. 12 discussed in Subsection IV.B indicate that under external stress the tip of the MN deforms plastically prior to the tip fracture, suggesting that the needle tip deforms gradually and loses its initial sharpness when being pressed against the porcine skin and prior to the successful insertion into skin. This gradual deformation of the needle tip blunts the tip.

Therefore, it is of importance to evaluate the tip-blunting force, which is defined as the external force being applied to an MN that makes the MN tip so blunt that successful

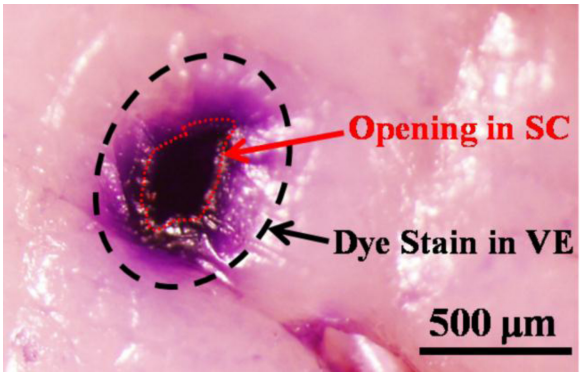


Fig. 17. An optical micrograph of the top view of an insertion site on the porcine skin following the insertion of the microneedle and the dye staining. The opening in the stratum corneum (SC) is caused by the successful insertion of the needle, followed by the dye flowing through the opening and staining the viable epidermis (VE) underneath.

TABLE I
SKIN STAINING RESULT IN THE TIP-BLUNTING FORCE TEST

| Sequence of Insertion / Test — Sample no. of MN | 1 | 2 | 3 |
|---|---|---|---|
| initial 50N insertion test | ✓ | ✓ | ✓ |
| first 50N re-insertion test | ✓ | ✓ | ✓ |
| second 50N re-insertion test | ✓ | ✓ | ✓ |
| third 50N re-insertion test | ✓ | ✓ | ✓ |
| remark | no significant tip deformation or fracture observed after all insertion tests | | |

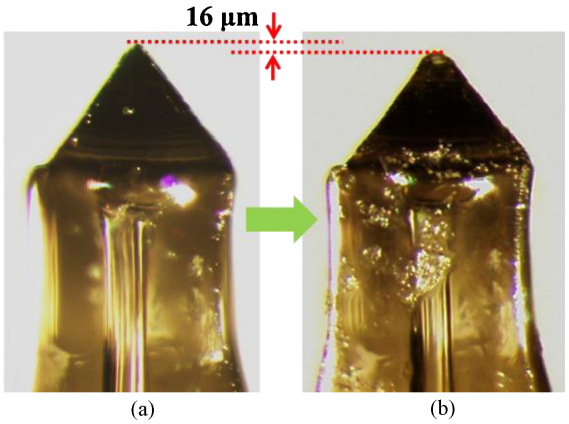


Fig. 18. Optical micrographs of the side view of a microneedle (a) before and (b) after the fracture test with the maximum driving force of 90 N against porcine skin. Minor plastic deformation of the needle tip is observed following the test.

insertion into skin cannot be made with the same external force. It is desirable that the tip-blunting force of the needle is significantly larger than the insertion force so that the MN inserts successfully into skin prior to being blunt that prevents successful insertion.

To estimate the tip-blunting force, an MN was pressed perpendicularly against the porcine skin at a rate of 1.0 mm/s by a force–displacement test station, Bose ElectroForce 3200 Test Instrument (Bose Co., Eden Prairie, MN, USA), followed by separation of the needle from the skin. Maximum driving force was set to be 50 N for each test. The 50 N force was chosen such that this force is approximately one order of magnitude higher than the maximum measured insertion force from the 15 insertion tests in Fig. 16, which is ∼4.5N. Skin staining test was then performed to verify the successful insertion of the needle into skin.

Three individual MNs were tested, and each needle was pressed against the porcine skin with the maximum driving force of 50 N in the initial insertion test and the following three re-insertion tests. After all four insertion tests, each needle tip was examined under an optical microscope.

The skin staining results for each insertion test are shown in Table I. With the maximum force of 50 N being applied to an MN in the initial insertion test as well as the first and second re-insertion tests, each of the three tested MNs remained capable of inserting successfully into porcine skin in the third re-insertion test. In addition, no significant tip deformation or fracture was observed under an optical microscope for all three MNs after four insertion tests.

These insertion tests indicate that for insertion into porcine skin the driving force that results in blunting the needle tip, i.e., the tip-blunting force, is larger than 50 N. Furthermore, the 50 N force is one-order-of-magnitude higher than the maximum measured insertion force for porcine skin. Therefore, with the tip-blunting force larger than 50 N and the maximum insertion force of 4.5 N, the margin of safety for successful needle insertion into porcine skin prior to significant tip blunting is greater than 10 [43].

4) *Fracture Force Estimation:* The intrinsic fracture of an MN against a rigid surface is discussed in Subsection IV.B. With potential applications of MNs for live animals and in clinic, the fracture force of the MN when being pressed against skin for insertion was characterized. Three individual needles were tested to estimate the fracture force against porcine skin using the apparatus described previously. Successful insertion of each needle into porcine skin was confirmed with the examination of the skin staining under an optical microscope following the insertion.

Minor plastic deformation of the needle tip was observed under an optical microscope following the test in two of the three MNs, and no significant deformation was observed in the third. Fig. 18a and Fig. 18b shows optical micrograph of one of the two needles with minor plastic deformation prior to and following the fracture test, respectively. A comparison of the two micrographs shows that the tip of the needle was plastically deformed with a vertical distance of 16 $\mu$m. Plastic deformation with a vertical distance of 30 $\mu$m was observed at the needle tip of the other MN.

In all three needles, no fracture of the MN was observed under an optical microscope, indicating that the fracture force of the needle for insertion into porcine skin is in excess of 90 N. Moreover, the maximum force produced by a human thumb has been empirically determined and reported in the literature to be 105 N [39].

## V. Conclusion

A polymer-based fabrication process using UV lithography into micromolds is proposed to construct a hollow MN array with a baseplate. Fabricated pyramidal-tip SU-8 MNs are 825 $\mu$m in height and 400 $\mu$m in width with a lumen opening of 120 $\mu$m in diameter. The tip diameter across the $10 \times 10$ needle array ranges from 15 to 25 $\mu$m. Microfluidic characterization indicates 20% of the lumens are well-defined.

Using UV lithography into micromolds allows complex 3-D structures to be defined with both the mask pattern in the lithography process and the topography of the micromold. In this paper, with a pre-constructed PDMS mold defining the tip of the MN, the shaft and lumen of the needle as well as a baseplate are all constructed with SU-8 in a dual exposure lithography process. This conventional UV lithography process is batch processing that is scalable for the manufacturing of MNs. Moreover, UV lithography and micromolding methods are expected to have low mass production costs.

Mechanical characterization shows the pyramidal tip of the fabricated MNs fractures against a rigid surface with a driving force of $12.0 \pm 0.8$ N. The insertion performance of MNs is evaluated with excised porcine skin. The driving force required for successful insertion of a MN into skin is empirically determined to be $2.4 \pm 1.2$ N. With the driving force increased to 50 N, the needle remains capable of successful insertion into skin with the same force after the first insertion is obtained. Moreover, the application of the 90 N force on a single needle causes minor tip deformation with no fracture observed under an optical microscope.

## Acknowledgments

The authors thank Dr. Jeong Woo Lee for the instruction on the Tricor force–displacement test station and Mr. James Norman for helpful discussion on the maximum human thumb force. Both Dr. Lee and Mr. Norman are in the Laboratory for Drug Delivery directed by Prof. Mark Prausnitz at the Georgia Institute of Technology.

## References

[1] M. R. Prausnitz, "Microneedles for transdermal drug delivery," *Adv. Drug Del. Rev.*, vol. 56, no. 5, pp. 581–587, Mar. 2004.

[2] Q. Zhu, V. G. Zarnitsyn, L. Ye, Z. Wen, Y. Gao, L. Pan, I. Skountzou, H. S. Gill, M. R. Prausnitz, C. Yang, and R. W. Compans, "Immunization by vaccine-coated microneedle arrays protects against lethal influenza virus challenge," in *Proc. Nat. Acad. Sci. U.S.A.*, vol. 106, no. 19. May 2009, pp. 7968–7973.

[3] H. S. Gill, J. Soderholm, M. R. Prausnitz, and M. Sallberg, "Cutaneous vaccination using microneedles coated with hepatitis C DNA vaccine," *Gene Therapy*, vol. 17, no. 6, pp. 811–814, Jun. 2010.

[4] P. Van Damme, F. Oosterhuis-Kafeja, M. Van der Wielen, Y. Almagor, O. Sharon, and Y. Levin, "Safety and efficacy of a novel microneedle device for dose sparing intradermal influenza vaccination in healthy adults," *Vaccine*, vol. 27, no. 3, pp. 454–459, Jan. 2009.

[5] A. Arora, M. R. Prausnitz, and S. Mitragotri, "Micro-scale devices for transdermal drug delivery," *Int. J. Pharmaceutics*, vol. 364, no. 2, pp. 227–236, Dec. 2008.

[6] M. R. Prausnitz, S. Mitragotri, and R. Langer, "Current status and future potential of transdermal drug delivery," *Nat. Rev. Drug Discovery*, vol. 3, no. 2, pp. 115–124, Feb. 2004.

[7] J. C. Birchall, R. Clemo, A. Anstey, and D. N. John, "Microneedles in clinical practice—An exploratory study into the opinions of healthcare professionals and the public," *Pharmaceutical Res.*, vol. 28, no. 1, pp. 95–106, Jan. 2011.

[8] S. M. Bal, Z. Ding, E. van Riet, W. Jiskoot, and J. A. Bouwstra, "Advances in transcutaneous vaccine delivery: Do all ways lead to Rome?" *J. Controlled Release*, vol. 148, no. 3, pp. 266–282, Dec.459 2010.

[9] A. Ovsianikov, B. Chichkov, P. Mente, N. A. Monteiro-Riviere, A. Doraiswamy, and R. J. Narayan, "Two photon polymerization of polymer-ceramic hybrid materials for transdermal drug delivery," *Int. J. Appl. Ceramic Technol.*, vol. 4, no. 1, pp. 22–29, 2007.

[10] Y. Choi, M. A. McClain, M. C. LaPlaca, A. B. Frazier, and M. G. Allen, "Three dimensional MEMS microfluidic perfusion system for thick brain slice cultures," *Biomed. Microdevices*, vol. 9, no. 1, pp. 7–13, Feb. 2007.

[11] S. A. Burton, F. L. Frederickson, K. J. Hansen, R. P. Simmers, P. T. Fenn, and C. S. Moeckly, "Hollow microneedle array and method," U.S. Patent Application 13/128,066, Nov. 2009.

[12] S. P. Davis, W. Martanto, M. G. Allen, and M. R. Prausnitz, "Hollow metal microneedles for insulin delivery to diabetic rats," *IEEE Trans. Biomed. Eng.*, vol. 52, no. 5, pp. 909–915, May 2005.

[13] H. J. G. E. Gardeniers, R. Luttge, E. J. W. Berenschot, M. J. de Boer, S. Y. Yeshurun, M. Hefetz, R. van't Oever, and A. van den Berg, "Silicon micromachined hollow microneedles for transdermal liquid transport," *J. Microelectromech. Syst.*, vol. 12, no. 6, pp. 855–862, Dec. 2003.

[14] B. Stoeber and D. Liepmann, "Two-dimensional arrays of out-of-plane needles," in *Proc. ASME Int. Mech. Eng. Congr. Expo.*, Orlando, FL, USA, 2000, pp. 355–359.

[15] B. Stoeber and D. Liepmann, "Arrays of hollow out-of-plane microneedles for drug delivery," *J. Microelectromech. Syst.,* vol. 14, no. 3, pp. 472–479, Jun. 2005.

[16] N. Roxhed, T. C. Gasser, P. Griss, G. A. Holzapfel, and G. Stemme, "Penetration enhanced ultrasharp microneedles and prediction on skin interaction for efficient transdermal drug delivery," *J. Microelectromech. Syst.*, vol. 16, no. 6, pp. 1429–1440, Dec. 2007.

[17] N. Baron, J. Passave, B. Guichardaz, and G. Cabodevila, "Investigations of development process of high hollow beveled microneedles using a combination of ICP RIE and dicing saw," *Microsyst. Technol.*, vol. 14, no. 9–11, pp. 1475–1480, 2008.

[18] F. Pérennès, B. Marmiroli, M. Matteucci, M. Tormen, L. Vaccari, and E. D. Fabrizio, "Sharp beveled tip hollow microneedle arrays fabricated by LIGA and 3D soft lithography with polyvinyl alcohol," *J. Micromech. Microeng.*, vol. 16, no. 3, pp. 473–479, 2006.

[19] S. Kuo and Y. Chou, "A novel polymer microneedle arrays and PDMS micromolding technique," *Tamkang J. Sci. Eng.*, vol. 7, no. 2, pp. 95–98, 2004.

[20] R. Luttge, E. J. W. Berenschot, M. J. de Boer, D. M. Altpeter, E. X. Vrouwe, A. van den Berg, and M. Elwenspoek, "Integrated lithographic molding for microneedle-based devices," *J. Microelectromech. Syst.*, vol. 16, no. 4, pp. 872–884, Aug. 2007.

[21] B. P. Chaudhri, F. Ceyssens, H. P. Neves, A. La Manna, C. Van Hoof, and R. Puers, "Out-of-plane high strength polymer microneedles for transdermal drug delivery," in *Proc. 33rd Annu. Int. Conf. IEEE Eng. Med. Biol. Soc.*, Boston, MA, USA, 2011, pp. 3680–3683.

[22] K. Lee, H. C. Lee, D. S. Lee, and H. Jung, "Drawing lithography: Three-dimensional fabrication of an ultrahigh-aspect-ratio microneedle," *Adv. Mater.*, vol. 22, no. 4, pp. 483–486, Jan. 2010.

[23] I. Mansoor, U. O. Hafeli, and B. Stoeber, "Hollow out-of-plane polymer microneedles made by solvent casting for transdermal drug delivery," *J. Microelectromech. Syst.*, vol. 21, no. 1, pp. 44–52, 2011.

[24] P.-C. Wang, B. A. Wester, S. Rajaraman, S.-J. Paik, S.-H. Kim, and M. G. Allen, "Hollow polymer microneedle array fabricated by photolithography process combined with micromolding technique," in *Proc. 31st Annu. Int. Conf. IEEE Eng. Med. Biol. Soc.*, Minneapolis, MN, USA, 2009, pp. 7026–7029.

[25] S. A. Campbell, *The Science and Engineering of Microelectronic Fabrication*, 2nd ed. New York, NY, USA: Oxford Univ. Press, 2001, pp. 151–182.

[26] T. C. Merkel, V. I. Bondar, K. Nagai, B. D. Freeman, and I. Pinnau, "Gas sorption diffusion and permeation in PDMS," *J. Polym. Sci.: Part B: Polym. Phys.*, vol. 38, no. 3, pp. 415–434, 2000.

[27] M. S. Rogalski and S. B. Palmer, *Advanced University Physics*. Boca Raton, FL, USA: CRC Press, 2005, pp. 411–428.

[28] B. H. Ong, X. Yuan, and S. C. Tjin, "Adjustable refractive index modulation for a waveguide with SU-8 photoresist by dual-UV exposure lithography," *Appl. Optics*, vol. 45, no. 31, pp. 8036–8039, 2006.

[29] S. Owega, D. Poitras, and K. Faid, "Solid-state optical coupling for surface plasmon resonance sensors," *Sens. Actuators B, Chem.*, vol. 114, no. 1, pp. 212–217, 2006.
[30] N. J. Giordano, *College Physics: Reasoning and Relationships*. Stamford, CT, USA: Cengage Learning, 2010, p. 448.
[31] A. Govindaraju, A. Chakraborty, and C. Luo, "Reinforcement of PDMS masters using SU-8 truss structures," *J. Micromech. Microeng.*, vol. 15, no. 6, pp. 1303–1309, 2005.
[32] R. Feng and R. J. Farris, "Influence of processing conditions on the thermal and mechanical properties of SU8 negative photoresist coatings," *J. Micromech. Microeng.*, vol. 13, no. 1, pp. 80–88, 2003.
[33] Y.-K. Yoon, J.-H. Park, F. Cros, and M. G. Allen, "Integrated vertical screen microfilter system using inclined SU-8 structures," in *Proc. IEEE 16th Annu. Int. Conf. Micro Electro Mech. Syst.*, Kyoto, Japan, 2003, pp. 227–230.
[34] J. Kim, M. G. Allen, and Y.-K. Yoon, "Computer-controlled dynamic mode multidirectional UV lithography for 3D microfabrication," *J. Micromech. Microeng.*, vol. 21, no. 3, p. 035003, 2011.
[35] S. Rajaraman, M. A. McClain, S. O. Choi, J. D. Ross, S. P. DeWeerth, M. C. LaPlaca, and M. G. Allen, "Three-dimensional metal transfer micromolded microelectrode arrays (MEAs) for in-vitro brain slice recordings," in *Proc. Transducers'07 Eurosensors XXI*, Lyon, France, 2007, pp. 1251–1254.
[36] S. Rajaraman, J. A. Bragg, J. D. Ross, and M. G. Allen, "Micromachined three-dimensional electrode arrays for transcutaneous nerve tracking," *J. Micromech. Microeng.*, vol. 21, no. 8, p. 085014, 2011.
[37] K. Wouters and R. Puers, "Diffusing and swelling in SU-8: Insight in material properties and processing," *J. Micromech. Microeng.*, vol. 20, no. 9, p. 095013, 2010.
[38] R. Yang and W. Wang, "A numerical and experimental study on gap compensation and wavelength selection in UV-lithography of ultra-high aspect ratio SU-8 microstructures," *Sen. Actuators B, Chem.*, vol. 110, no. 2, pp. 279–288, 2005.
[39] Z. Li and R. J. Goitz, "Biomechanical evaluation of the motor function of the thumb," *Technol. Health Care*, vol. 11, no. 4, pp. 233–243, 2003.
[40] M. A. Meyers and K. K. Chawla, *Mechanical Behavior of Materials*, 1st ed. Upper Saddle River, NJ, USA: Prentice-Hall, 1998, pp. 412–416.
[41] S. D. Senturia, *Microsystem Design*. Norwell, MA, USA: Kluwer Academic Publishers, 2001, pp. 196–197.
[42] S. P. Davis, B. J. Landis, Z. H. Adams, M. G. Allen, and M. R. Prausnitz, "Insertion of microneedles into skin: Measurement and prediction of insertion force and needle fracture force," *J. Biomechanics*, vol. 37, no. 8, pp. 1155–1163, Aug. 2004.
[43] J. M. Gere and B. J. Goodno, *Mechanics of Materials*, 8th ed. Stamford, CT, USA: Cengage Learning, 2012, pp. 68–69.

**Po-Chun Wang** received the B.S. degree in electronics engineering from National Chiao-Tung University, Hsin-Chu, Taiwan, in 1997, and the M.S. degree in electrical engineering from Pennsylvania State University, State College, PA, USA, in 2002. From 2002 to 2007, he was with Taiwan Semiconductor Manufacturing Company, Hsin-Chu, Taiwan, where he enhanced yield and performance of silicon CMOS integrated circuits. He is currently pursuing the Ph.D. degree in electrical and computer engineering at the Georgia Institute of Technology, Atlanta, GA, USA. His current research interests include fabrication and characterization of micromachined hollow polymer needle arrays for drug delivery into skin.

**Seung-Joon Paik** received the B.S. degree from the School of Electrical Engineering and the M.S. and Ph.D. degrees from the Department of Electrical Engineering and Computer Science, Seoul National University, Seoul, Korea, in 1999, 2001, and 2005, respectively. His Ph.D. dissertation was focused on design, microfabrication, and testing of silicon microneedles for neurophysiologic applications, including microfluidic channels and microelectrodes. He was with the Automation and Systems Research Institute at Seoul National University, as a Post-Doctoral Fellow from 2005 to 2007, where he developed inertial sensors and systems for robot localization and locomotion applications. He was also with SML Electronics, Inc., Seoul, from 2007 to 2008, where he developed wafer-level packaging and manufacturing processes of MEMS accelerometers and gyroscopes. He is currently a Post-Doctoral Fellow with the School of Electrical and Computer Engineering of the Georgia Institute of Technology, Atlanta, GA, USA. His current research interests include micromachining of silicon and polymer materials and in biomedical applications of micromachined devices. Other research interests include inertial sensors, 3-D multichip packaging of MEMS devices, energy storage/conversion devices, and nano-scale structures.

**Shuodan Chen** received the B.S. degree in electrical engineering from the Georgia Institute of Technology (Georgia Tech), Atlanta, GA, USA, in 2003. From 2003 to 2006, after garnering the National Science Foundation Graduate Fellowship, she completed the M.S. and Ph.D. degrees in electrical engineering from the Massachusetts Institute of Technology (MIT), Cambridge, MA, USA. Her graduate research work at the MIT Center of Biomedical Engineering focused on the impact of injury on knee cartilage surface as it leads to osteoarthritis. The findings were presented in *Arthritis and Rheumatism* in 2009, the Annual Orthopedic Research Society Conference from 2006 to 2010, and the Osteoarthritis Research Society International Conference in 2009. Shuodan returned to Georgia Tech for Post-Doctoral work at the Institute of Electronics and Nanotechnology. One project there involved designing, building, and validating an applicator-package for controlled transdermal microneedle array insertion. The second project included incorporating planar fabrication techniques of natural materials into neuroelectrode fabrication for biocompatibility during cortical sensing. In conjunction with the neuroelectrode project, she also completed a review article for *the Materials Research Society Bulletin* in 2012.

**Swaminathan Rajaraman** received the B.S. degree in electronics engineering from Bharathidasan University, Trichy, India, the M.S. degree in electrical engineering from the University of Cincinnati, Cincinnati, OH, USA, and the Ph.D. degree in Electrical Engineering from the Georgia Institute of Technology, Atlanta, GA, USA, in 1998, 2001, and 2009, respectively.

From 2001 to 2002, he was with the Analog Devices Micromachined Products Division (MPD) in Cambridge, MA, USA, where he developed optical MEMS micro-mirrors for telecommunication applications. From 2004 to 2005, he was with CardioMEMS in Atlanta, where he developed implantable MEMS pressure sensors for detection of heart disease. Since 2007, he has been with Axion BioSystems, Atlanta, where he currently holds the title of VP, Biological and Materials Engineering. His current research interests include *in vitro* and *in vivo* microelectrode arrays (MEAs), micro/nanofabrication, microneedles, microtweezers, micro-TAS, nanosensors, and implantable MEMS devices. Dr. Rajaraman was the track chair for the Bioelectric Sensors session in IEEE EMBC 2010.

**Seong-Hyok Kim** received the B.S.E. and M.S. degrees from the Department of Electrical Engineering, Seoul National University, Seoul, Korea, in 1996 and 1998, respectively. He received the Ph.D. degree in electrical engineering and computer science from Seoul National University in 2002. After joining the LG Electronics Institute of Technology as a Senior Research Engineer in 2002, he participated in the design and fabrication of a wide variety of MEMS devices for portable electronics. In 2005, Dr. Kim joined the Micro Sensors and Micro Actuators Laboratory (MSMA) at the Georgia Institute of Technology, Atlanta, GA, USA, as a Post-Doctoral Fellow and led the PowerMEMS research group at the MSMA lab. Since he became a Research Engineer II in 2007, Dr. Kim has led the MSMA laboratory's research projects encompassing micro sensors and actuators, nanomaterials, power passives, bio-medical microdevices, etc. Since 2010, he has been the Principal Research Engineer at the LG Electronics Mobile Communication Company and has been leading an emerging core technology team on MEMS sensors. Dr. Kim has published more than 50 peer-reviewed journal and conference articles and holds 29 Korean/International patents in the field of MEMS including power MEMS, bio MEMS, polymer MEMS, optical MEMS, and MEMS sensors and actuators.

**Mark G. Allen** (M'89–SM'04–F'11) received the B.A. degree in chemistry, the B.S.E. degree in chemical engineering, and the B.S.E. degree in electrical engineering from the University of Pennsylvania, Philadelphia, PA, USA, and the S.M. and Ph.D. degree from the Massachusetts Institute of Technology, Cambridge, MA, USA. In 1989, he joined the faculty of the School of Electrical and Computer Engineering of the Georgia Institute of Technology, Atlanta, GA, USA, where he currently holds the rank of Regents' Professor and the J.M. Pettit Professorship in Microelectronics, as well as a joint appointment in the School of Chemical and Biomolecular Engineering. His current research interests include the development and application of new micro- and nanofabrication technologies, as well as MEMS. He is Editor-in-Chief of the *Journal of Micromechanics and Microengineering* and the former Co-Chair of the IEEE/ASME MEMS Conference.